

**1 Electron Backscatter in Energetic Particle
2 Precipitation: Data Analysis and Simulation**

3 Julia Luna Claxton¹, Robert Marshall¹

4¹Ann and H. J. Smead Department of Aerospace Engineering Sciences, University of Colorado Boulder
5¹Boulder, CO, USA

6 Key Points:

- 7**• The rate of atmospheric backscatter of radiation belt electrons is constrained us-
8 ing data collected from low-Earth orbit.
- 9**• An improved Monte Carlo model is used to simulate electron-atmosphere inter-
10 actions and is validated using the same in-situ data.
- 11**• The sensitivity and pitch angle distributions of backscattered populations are char-
12 acterized using this new Monte Carlo model.

13 **Abstract**

14 When particles from the radiation belts impinge on the atmosphere, they can be absorbed
 15 into the atmosphere or deflected back into the magnetosphere. The deflection of parti-
 16 cles back into the magnetosphere is known as backscatter, and is a key link connecting
 17 the atmosphere to the magnetosphere involving collisions with atmospheric neutrals, mag-
 18 netic mirroring, the production of secondary emissions, and energy transfer from the par-
 19 ticle to the atmosphere. Backscatter is both a feedback mechanism to magnetospheric
 20 precipitation drivers and an indirect measure of atmospheric energy absorption, mak-
 21 ing it an important process to quantify and understand.

22 In this work, we use data from the Electron Fields and Losses INvestigation (ELFIN)
 23 satellites to quantify backscatter rates. We find that backscatter rates vary between \sim
 24 5% during periods of loss cone filling and \sim 60% during periods without loss cone fill-
 25 ing. We then compare the ELFIN backscatter data to the results of an updated and im-
 26 proved Monte Carlo-based simulation and find excellent agreement for the mean backscat-
 27 ter rates. Errors in backscatter predictions on a case-by-base basis are attributed to in-
 28 sufficient pitch angle resolution in the in-situ data along with high sensitivity of backscat-
 29 ter to pitch angle near the loss cone edge. Finally, we use our improved Monte Carlo model
 30 to characterize the pitch angle and energy dependence of backscatter and the pitch an-
 31 gle distributions of backscattered electrons, finding results consistent with previous mod-
 32 eling efforts.

33 **Plain Language Summary**

34 Near-Earth space is filled with high-energy radiation moving in a variety of differ-
 35 ent directions. When this radiation impacts the Earth's atmosphere, we can experience
 36 a number of adverse effects, including the depletion of the ozone layer and disruptions
 37 to telecommunications and power distribution. The Earth's atmosphere and magnetic
 38 core help deflect this radiation, but it is not currently known exactly what percentage
 39 of incoming radiation breaches these defenses and is deposited in the atmosphere.

40 In this paper, we use a radiation detector on an Earth-orbiting satellite to deter-
 41 mine exactly how much radiation the Earth's atmosphere and magnetic field repels. We
 42 find that the amount of radiation repelled depends on the angle at which the radiation
 43 approaches the Earth. Only about 5% of radiation that is directed straight at the Earth
 44 gets repelled, while up to 60% of incoming radiation at shallower angles is repelled. We
 45 then use computer simulations to find that the Earth's atmosphere is responsible for re-
 46 peling the direct radiation, while the Earth's magnetic field is responsible for repelling
 47 the radiation at shallow angles.

48 Studying how often and by what method spaceborne radiation is repelled helps us
 49 prepare for extreme events such as solar storms more effectively by allowing us to fore-
 50 cast how much of the radiation they emit will reach crucial infrastructure systems on the
 51 ground, since solar storms can alter the angle that radiation approaches the Earth at.
 52 The information in this paper allows space weather forecasters to better predict and mit-
 53 igate the effects of space radiation impacting the Earth.

54 **1 Introduction**

55 Energetic particle precipitation (EPP) is the process where charged particles from
 56 the Earth's magnetosphere collide with the atmosphere. In this process, particles either
 57 deposit their energy in the atmosphere or are deflected back into the magnetosphere via
 58 magnetic mirroring and collisions with atmospheric neutrals. Atmospheric deposition
 59 of energetic particles causes cascade effects such as the production of odd hydrogen and
 60 odd nitrogen that can in turn reduce ozone concentrations in the stratosphere (Randall

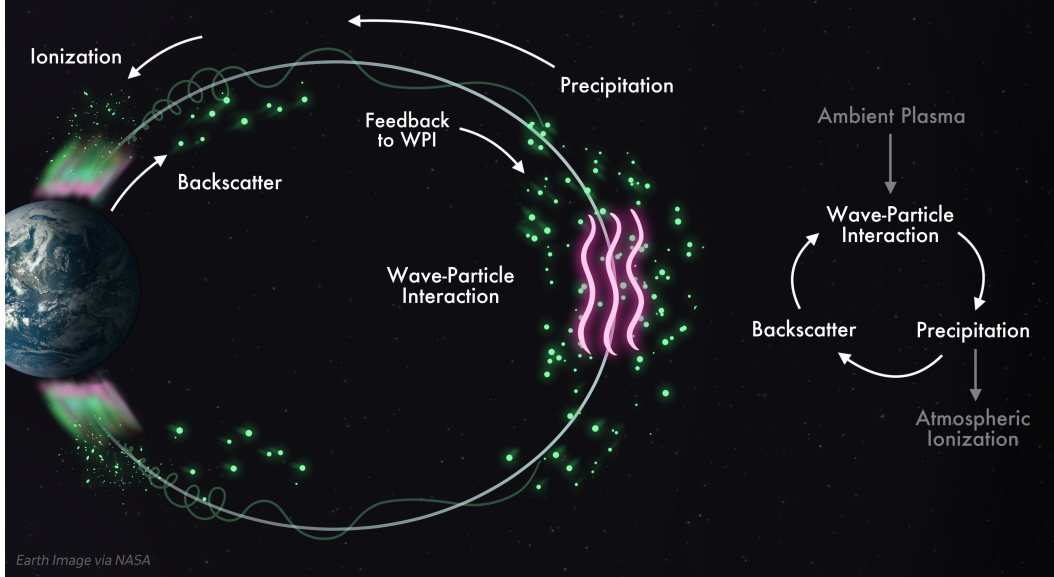


Figure 1. Schematic representation of the interconnected magnetosphere-atmosphere system. Backscatter is a key component of this system, acting as a feedback mechanism that closes the loop between the atmosphere and magnetosphere.

et al., 2005; Seppälä et al., 2007; Sinnhuber et al., 2012; Funke et al., 2014; Koskinen & Kilpua, 2022). Additionally, EPP is a central loss process for the radiation belts (Ripoll et al., 2020; Millan & Thorne, 2007). The deflection, or scattering, of precipitating particles back into the magnetosphere is known as backscatter. Backscatter is an important process in the magnetosphere, serving both as a feedback mechanism that directly shapes the characteristics of many observed precipitation patterns – such as bouncing packets, diffuse aurora, and lightning-induced electron precipitation (Feinland et al., 2024; Wetzel et al., 2024; Khazanov & Chen, 2021; Cotts et al., 2011; Davidson & Walt, 1977) – and as an indirect measure of atmospheric energy absorption due to EPP. However, until recently, no datasets have been produced with sufficient angular resolution to quantify backscatter on a global scale. This deficiency has been overcome in recent years with the launch of the Electron Losses and Fields INvestigation (ELFIN) mission (Angelopoulos et al., 2020).

In this paper, we quantify the rates of EPP backscatter using data from the ELFIN satellites; compare those results with simulations using an updated and improved Monte Carlo-based EPP model and evaluate the model’s performance at predicting backscatter; and use our model to characterize the energy and pitch angle characteristics of backscatter.

2 Background

The existence of backscatter has been known for nearly as long as the radiation belts themselves. In the early 1960s, a sounding rocket experiment measured upgoing auroral fluxes with nearly the same intensity as downgoing fluxes in the lower thermosphere (~ 100 km) (McDiarmid et al., 1961), sparking interest in the phenomenon. Backscatter was observed on spaceborne platforms shortly after, with backscatter ratios (backscattered flux divided by precipitating flux) observed on the order of 10% (O’Brien, 1962, 1964). Further interest was generated by Cummings et al. (1966) with the discovery that backscatter showed a dependence on precipitating flux, ranging from approximately 20%

88 at high fluxes to nearly 100% at low fluxes. Richards and Peterson (2008) used data from
 89 the FAST satellite, finding backscatter ratios for sub-100 keV electrons in the range of
 90 approximately 25% at 100 keV up to nearly 100% in the sub-eV range. The high backscat-
 91 ter for lower energy channels indicates a softening of precipitating particle energy spec-
 92 tra.

93 On the theoretical side, a number of simulation studies have been conducted to bet-
 94 ter understand EPP backscatter (Maeda, 1965; Cummings et al., 1966; Walt et al., 1968;
 95 P. Banks & Nagy, 1970; P. M. Banks et al., 1974; Berger et al., 1974; Mantas & Walker,
 96 1976; Davidson & Walt, 1977; Lejeune, 1979; Cotts et al., 2011; Marshall & Bortnik, 2018;
 97 Berland et al., 2023). Techniques for both simulating and reporting backscatter statis-
 98 tics vary from author to author. For example, early models (Maeda, 1965; Berger et al.,
 99 1974) did not incorporate the effect of magnetic mirroring. Some studies analyzed backscat-
 100 ter as a function of pitch angle (Berger et al., 1974; Cotts et al., 2011; Marshall & Bort-
 101 nik, 2018; Berland et al., 2023), but many opted to study the backscatter of predefined
 102 pitch angle distributions as a function of energy, thus neglecting a key sensitivity (Maeda,
 103 1965; Cummings et al., 1966; Walt et al., 1968; P. Banks & Nagy, 1970; P. M. Banks et
 104 al., 1974; Mantas & Walker, 1976; Solomon, 2001). In addition to differences in simu-
 105 lation procedure, a number of different quantities have been referred to as "backscatter",
 106 further complicating comparisons (Mantas & Walker, 1976). A comprehensive simula-
 107 tion of backscatter incorporating a realistic magnetic field without prescribed input pitch
 108 angle or energy distributions for electrons would not come until Cotts et al. (2011), fol-
 109 lowed by Marshall and Bortnik (2018) and Berland et al. (2023).

110 Despite the inconsistencies in simulation and reporting, some general trends emerge
 111 from the literature. First, we note that backscatter ratios inside the trapped region are
 112 significantly lower in simulations that do not incorporate magnetic mirroring, indicat-
 113 ing that mirroring is a critical process in shaping the bounce loss cone. Second, the en-
 114 ergy spectrum of backscattered populations is much softer (skewed toward lower ener-
 115 gies) than the incoming spectrum, with backscattered fluxes often exceeding downgo-
 116 ing fluxes in low-energy regimes due to the effect of high-energy particles being backscat-
 117 tered at lower energies. This effect is responsible for the near-100%, and sometimes greater
 118 than-100%, backscatter ratios observed in-situ (e.g. McDiarmid et al. (1961); Cummings
 119 et al. (1966); Richards and Peterson (2008)). Additionally, we notice a trend of gener-
 120 ally higher backscatter ratios being predicted and observed at lower precipitating fluxes.
 121 Finally, we note that interaction with the atmosphere serves to diffuse a pitch angle dis-
 122 tribution with the intensity of diffusion increasing as the input pitch angle distribution
 123 becomes more field-aligned.

124 Backscatter plays a role in shaping a number of precipitation patterns (Wetzel et
 125 al., 2024; Khazanov & Chen, 2021; Cotts et al., 2011; Davidson & Walt, 1977). However,
 126 it remains an understudied phenomenon in part due to a lack of data with sufficient res-
 127 olution to accurately constrain it for radiation belt electrons. Direct measurement of EPP
 128 distributions in the loss and anti-loss cone has been limited by instrument field-of-view
 129 and pitch angle resolution compared to the loss cone width (e.g. RBSP) or instrument
 130 attitude relative to the geomagnetic field (e.g. POES). Ground-based measurements of
 131 EPP (e.g. PFISR) cannot determine incoming EPP distributions without the use of in-
 132 version methods (Juarez Madera et al., 2023; Sanchez et al., 2022; Turunen et al., 2016;
 133 Miyoshi et al., 2015). With modern data from low-Earth orbit, however, we now have
 134 the tools to both comprehensively quantify backscatter rates and validate backscatter
 135 models.

136 3 Data Source: ELFIN

137 The Electron Losses and Fields Investigation (ELFIN) mission was a pair of twin
 138 CubeSats that launched in 2018 into a polar low-Earth orbit with ~ 450 km altitude

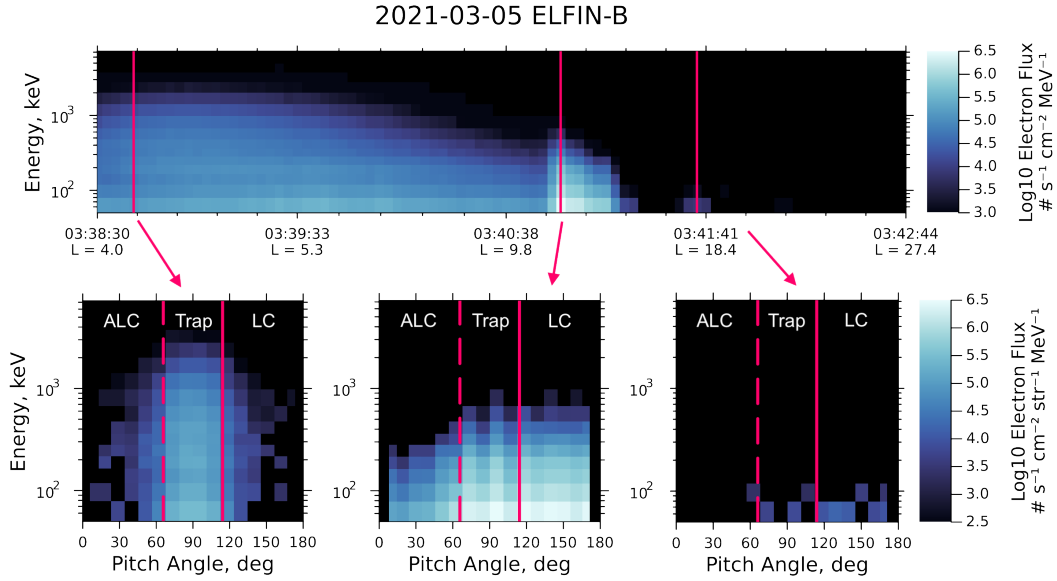


Figure 2. Example data collected from ELFIN. Top: Differential omnidirectional electron number flux as a function of time. Solid red lines indicate the selected timesteps of the bottom panels. Bottom: Differential directional electron number fluxes at selected timesteps. Solid red lines indicate the pitch angle of the 100 km loss cone (“LC”) and dashed red lines indicate the pitch angle of the conjugate anti-loss cone (“ALC”), both calculated using IGRF (Angelopoulos et al., 2020). The trapped region is marked as “Trap”. This pass was recorded in the southern hemisphere, thus the loss cone angle is greater than 90° . All times are given in UTC.

and $\sim 93^\circ$ inclination. The satellites had 16 energy channels approximately logarithmically spaced between 50 keV to 6 MeV. The electron detector had a field of view of $\sim 22.5^\circ$ that swept over a full rotation approximately every 2.8 seconds via spacecraft spin. The pitch angle coverage of each spin was dependent on the angle between the spacecraft spin axis and the local magnetic field. The spacecraft spin provided energy- and pitch-angle resolved fluxes during the ELFIN data collection periods discerning the loss cone, trapped region, and anti-loss cone in unprecedented detail (Angelopoulos et al., 2020). During ELFIN’s science collection periods, the loss cone width, assuming a mirror altitude of 100 km, was approximately 67° in the Northern hemisphere and approximately 113° in the Southern hemisphere. An example of ELFIN data from the Southern hemisphere is shown in Figure 2. The top panel shows omnidirectional differential electron flux recorded by ELFIN over time yielded by multiplying the recorded fluxes at each timestep by ELFIN’s solid angle field of view and summing over pitch angle. The bottom panels show the flux measured at three selected timesteps as a function of energy and pitch angle without any integration applied. The loss cone angle is marked with a solid line and the label “LC”. The anti-loss cone angle is marked a dashed line and the label “ALC”. The trapped region lies between these two lines and is labelled “Trap”. The first panel shows ambient fluxes in the outer radiation belt; the second panel, measured in the current sheet, shows an example of pitch angle scattering due to field line curvature into the loss cone with significant backscatter; and the third panel shows a quiet distribution in the polar cap with very little flux.

160 3.1 Data Selection

161 For our analysis, all ELFIN data were divided into segments lasting 3 spacecraft
 162 spin periods (~ 8 seconds; ~ 24 km along track) each. This spin-averaging was done
 163 to smooth the data, as ELFIN has occasional artifacts that can be alleviated via inte-
 164 gration over multiple spins. Each 3-spin segment was then either discarded or retained
 165 for analysis based on its pitch angle coverage. A data segment was kept if it had con-
 166 tinuous pitch angle coverage between 5° and 175° , determined using the ELFIN Ener-
 167 getic Particle Detector's nominal field of view of 22.5° (Angelopoulos et al., 2020). This
 168 selection criteria ensures that no more than 10° of the pitch angle distribution (≈ 0.05 str)
 169 are unrecorded. If any portion of the data segment fell within a period of unreliable data,
 170 as provided on the ELFIN data website, the segment was discarded. A known type of
 171 corrupted data where all pitch angle look directions measured a uniform high flux was
 172 also removed by discarding any data segment with loss cone flux greater than $10^{4.5}$ electrons-
 173 $\text{cm}^{-2}\text{-s}^{-1}$ and number backscatter ratio (see Section 4 for backscatter ratio calculation)
 174 greater than 85%. Noise was then removed within each remaining data segment by ze-
 175 roing out any data points with relative error greater than 50%, where relative error was
 176 computed by the ELFIN team as Poisson noise using Equation 1 (Tsai, 2025). In Equa-
 177 tion 1, $\frac{\delta q}{q}$ is the relative error in a given measurement, and N_{counts} is the total number
 178 of counts the electron detector recorded during the measurement. After applying these
 179 conditions to the lifetime of both ELFIN satellites, we were left with 201 hours (254,838
 180 spacecraft spins) of data collected over 2 years. This dataset will be further downselected
 181 after the quantification of backscatter in Section 4 to only retain the highest quality seg-
 182 ments.

$$\frac{\delta q}{q} = \frac{1}{\sqrt{N_{\text{counts}}}} \quad (1)$$

183 4 ELFIN Backscatter Rates

184 In this work, we define the number backscatter ratio r_N as the number of parti-
 185 cles backscattered divided by the number of precipitating particles. Similarly, we define
 186 the energy backscatter ratio r_E as the amount of backscattered energy divided by the
 187 amount of precipitating energy (Equation 2). In ELFIN data, we define input fluxes as
 188 any fluxes within the 100 km bounce loss cone and backscattered fluxes as any fluxes within
 189 the conjugate anti-loss cone.

$$r_N = \frac{\#_{\text{ALC}}}{\#_{\text{LC}}} \quad r_E = \frac{E_{\text{ALC}}}{E_{\text{LC}}} \quad (2)$$

190 Backscatter rates were derived from the ELFIN data segments via the following
 191 procedure. Each data segment was divided into loss cone and anti-loss cone regions based
 192 on the central pitch angle of ELFIN's look directions during the segment. Since ELFIN's
 193 particle detector field of view is $\sim 22.5^\circ$ wide (Angelopoulos et al., 2020), it was deter-
 194 mined that a look direction's boresight angle must be more than 16.25° away from the
 195 loss or anti-loss cone edge, leaving a 5° gap between the edge of ELFIN's field of view
 196 and the loss & anti-loss cone edge in order to ensure no particles from the trapped re-
 197 gion were counted. The loss and anti-loss cone angles were calculated as the pitch an-
 198 gles having 100 km mirror altitudes using IGRF (Angelopoulos et al., 2020; Tsai, 2025);
 199 this angle varies geographically by a few degrees over the L ranges probed by ELFIN.
 200 Each look direction satisfying these constraints for the loss cone and anti-loss cone was
 201 then integrated over energy, pitch angle, area, and time to retrieve the total electron counts
 202 and total energy recorded in the loss cone and anti loss cone. The backscatter ratios r_N
 203 and r_E were calculated per Equation 2.

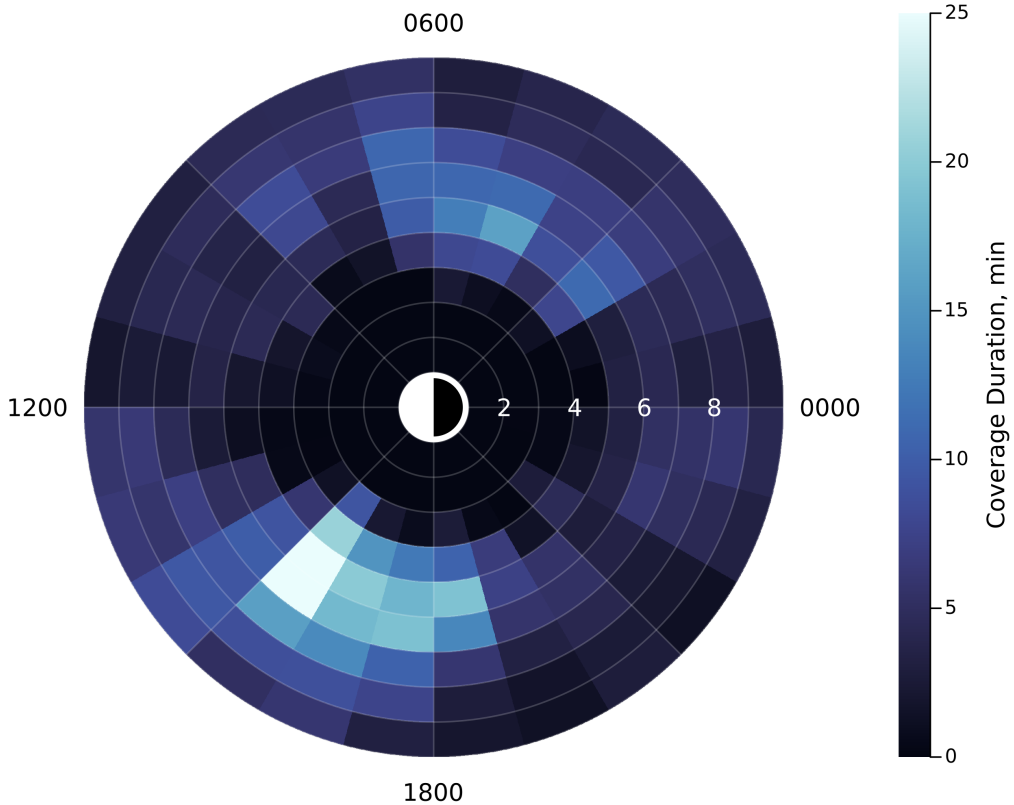


Figure 3. L-MLT coverage of the ELFIN dataset from which we will calculate backscatter ratios. This dataset encompasses 26 hours (33,366 spacecraft spins) of ELFIN data collected over 2 years. L and MLT are calculated using the T87 magnetic field model.

After the backscatter ratio was calculated for a given data segment, the error was found by propagating the relative error in the flux measurement at each time, energy, and pitch angle (Equation 1) through the steps taken to calculate the backscatter ratios. Any value of r_N or r_E with absolute uncertainty greater than $\sigma \approx 0.025$ was discarded. The discarded data is not necessarily unreliable – we are simply being very strict in our selection criteria to ensure the backscatter ratios we analyze are the highest-quality data ELFIN has to offer. This selection criteria resulted in a set of backscatter ratios derived from 26 hours (33,366 spacecraft spins) of data collected over 2 years. The coverage of this data in L-shell and magnetic local time (MLT) calculated using the T87LONG magnetic field model (Tsyganenko, 1987) is shown in Figure 3. The backscatter ratios calculated from this dataset are shown in Figure 4.

The data-derived backscatter distribution in Figure 4 demonstrates three notable features, from left to right in the figure: i) low backscatter ratios at low loss cone fluxes; ii) backscatter rates spanning low and high rates at medium fluxes; and iii) low backscatter ratios at high fluxes.

First we consider the low backscatter ratios at low loss cone fluxes ($\lesssim 10^{3.25}$ electrons-cm $^{-2}$ -s $^{-1}$). This is not a physical phenomenon, but rather a representation of our error propagation scheme and ELFIN's particle detector sensitivity. Since we are utilizing Poisson noise statistics to determine the uncertainty in the ELFIN measurements (Equation 1), lower fluxes have higher uncertainty. In this region, the fluxes in the loss cone just barely clear our uncertainty threshold to be included in the analysis. Even a small

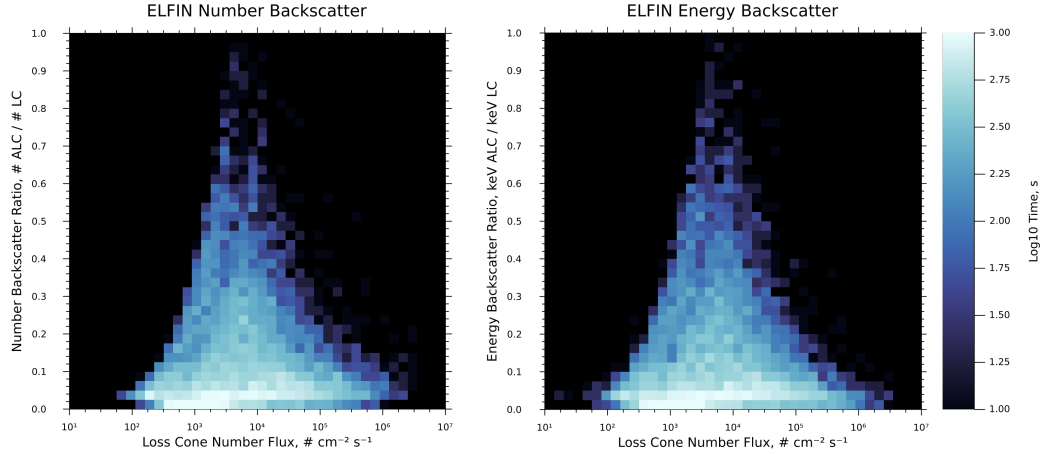


Figure 4. Backscatter ratios derived from 26 hours (33, 366 spacecraft spins) of ELFIN data. Backscatter ratio is defined as the total electron number or energy measured in the anti-loss cone divided by the total number or energy measured in the loss cone. Any measurement of backscatter ratio with absolute uncertainty greater than $\sigma \approx 0.025$ was discarded.

reduction in these fluxes due to interaction with the atmosphere is sufficient to push backscattered fluxes below our uncertainty threshold, whereupon we zero out the backscatter readings for these inputs. In this manner, backscattered particles are missed by falling below ELFIN's noise floor, creating backscatter ratios with artificially low values for these fluxes.

At high fluxes ($\gtrsim 10^5 \# \text{cm}^{-2} \text{s}^{-1}$), we see backscatter ratios in the range of approximately $r_N \in [5\%, 20\%]$ and $r_E \in [0\%, 15\%]$. This likely indicates a low rate of backscatter deep in the loss cone. This is because high loss cone fluxes indicate filling via pitch angle scattering (including curvature scattering) processes, which isotropizes the pitch angle distribution and fills the loss cone. The magnetic mirror force is less effective for these more field-aligned particles, sending them deeper into the atmosphere, causing them to be backscattered at lower rates. At this flux level in the loss cone, this pitch angle-scattered population greatly exceeds any ambient populations. Thus, the backscatter ratio for these pitch angle-scattered particles dominates, creating the lower backscatter rates we observe at high loss cone fluxes.

At medium fluxes (between approximately $10^{3.25} \# \text{cm}^{-2} \text{s}^{-1}$ and $10^5 \# \text{cm}^{-2} \text{s}^{-1}$), we see a spreading of the distribution with backscatter ratios of approximately $r_N, r_E \in [5\%, 70\%]$. We believe the lower backscatter ratios ($\lesssim 20\%$) in this range are due to particles scattered into the loss cone, as described previously. We believe the higher backscatter ratios ($\gtrsim 50\%$) indicates much higher backscatter rates near the loss cone edge. When this population is isolated – i.e. when there is weaker pitch-angle scattering – we see much higher backscatter ratios, since any particles deep in the loss cone are lost quickly without a refilling process. This leaves behind only particles near the loss cone edge, indicating that backscatter rates near the loss cone edge can be much higher than the rates at more field-aligned angles. We validate this conjecture in Section 7. Finally, we believe the intermediate range between the high and low backscatter values represent various strengths of pitch angle scattering causing a weighted mix between the high ambient backscatter rates and the lower pitch angle scattering-induced backscatter rates.

If our interpretation of this pattern is correct, we should observe a decreasing backscatter ratio with increased filling of the loss cone and high backscatter rates observed at times with less filling of the loss cone. If we use the ratio of precipitating flux over trapped flux

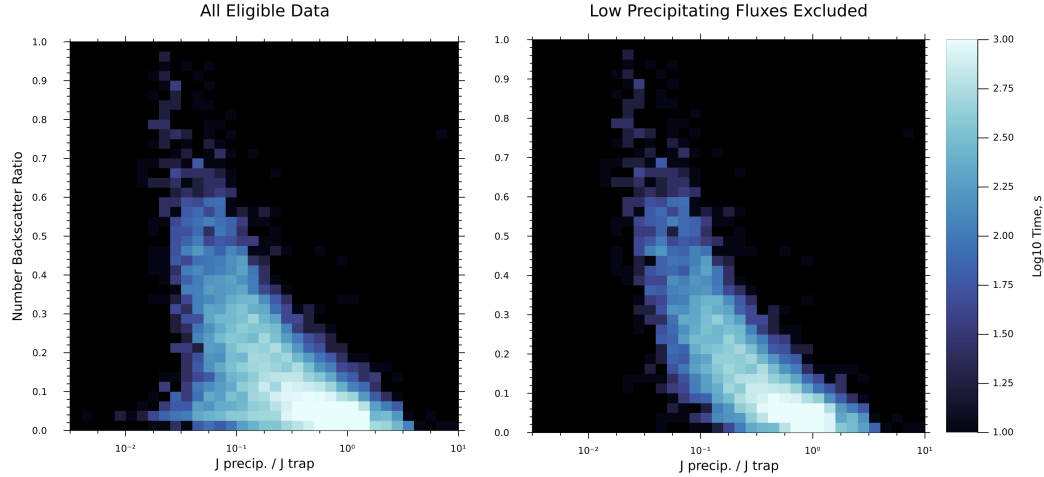


Figure 5. Number backscatter ratio vs. loss cone filling strength derived from 26 hours (33,366 spacecraft spins) of ELFIN data. Any measurement of backscatter ratio with absolute uncertainty greater than $\sigma \approx 0.025$ was discarded. Left: Results using data as previously described. Right: Measurements with precipitating flux less than $10^{3.5}$ electrons-cm $^{-2}$ -s $^{-1}$ removed to avoid artificially lowered backscatter ratios due to backscattered fluxes falling below the instrument noise floor. Energy backscatter ratio has a similar pattern to number backscatter ratio and is not shown for brevity.

as a measure of pitch angle distribution isotropization, and thereby loss cone filling (e.g. Capannolo et al. (2023)), we indeed observe this pattern (Figure 5, left). Recalling that low loss cone fluxes cause artificially low backscatter ratios, we remove measurements with loss cone fluxes below $10^{3.25}$ electrons-cm $^{-2}$ -s $^{-1}$ and find a clear pattern confirming our interpretation (Figure 5, right). A fit of the curve in 5 can be found in the Supporting Information.

Additionally, visual inspection of individual data segments at various backscatter levels support the conclusion that high backscatter ratios are present during times of ambient precipitation (i.e. no loss cone filling), low backscatter ratios are seen during times where the loss cone is filled, and intermediate backscatter ratios occur during the in-between cases. Example ELFIN data for each of these situations is shown in Figure 6. The left panel shows the case of ambient populations with an unfilled loss cone, where the majority of precipitating flux resides just inside the loss cone edge. This case has a high backscatter ratio of $r_N = 0.72$, indicating the high backscatter ratios in the region near the loss cone edge. The center panel shows the case of strong loss cone filling. Here, the fluxes reside significantly deeper into the loss cone, with significant fluxes reaching field-aligned angles. This case shows very little backscatter with $r_N = 0.05$, indicating that the backscatter rates deep in the loss cone are much lower than pitch angles near the loss cone. Finally, the right panel shows a data segment with an intermediate backscatter ratio of $r_N = 0.31$, showing a blend of the characteristics of the left and center panels. Some loss cone filling can be observed, but it is not as extreme as the center panel. Thus, we conclude that the dependence of backscatter ratio on loss cone filling indicates the underlying sensitivity of backscatter to pitch angle, with pitch angles near the loss cone edge having high backscatter ratios, transitioning to near-zero backscatter ratios at field-aligned angles.

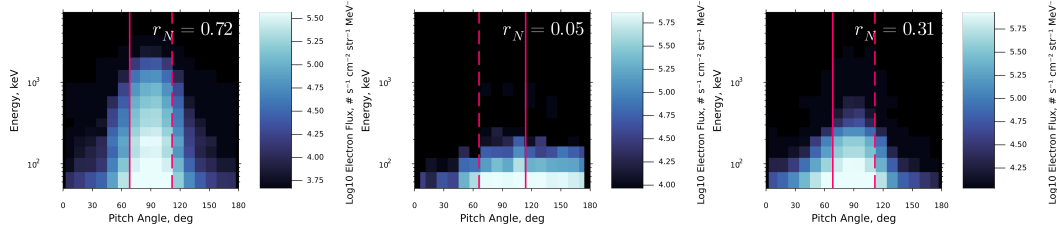


Figure 6. ELFIN-measured fluxes for data segments at three different levels of backscatter.

Left: A data segment with little filling of the loss cone and high backscatter ratio. Center: A data segment with strong loss cone filling and low backscatter ratio. Right: A data segment with partial loss cone filling and an intermediate backscatter ratio. Solid lines indicate the pitch angle of the 100 km loss cone, and dashed lines indicate the conjugate anti-loss cone pitch angle. The center panel was recorded in the Southern hemisphere, thus $\alpha_{LC} > \alpha_{ALC}$.

Parameter	Berland 2023	This Work
Physics List	QBBC	QBBC
Statistical Biasing	100x Bremsstrahlung Splitting	None
Magnetic Field	Uniform	Centered Dipole
Magnetic Latitude	65.77°	65.77°
Electron Injection Altitude	300 km	449.5 km
Electron Collection Altitude	500 km	450.5 km
Minimum Measurable Electron Energy	0.1 keV	0.01 keV
Atmosphere Model	NRLMSISE00	NRLMSISE00
Atmosphere Resolution	1 km	1 km
Atmosphere Model Time	2018-01-01 03:00:00 UTC	2018-01-01 03:00:00 UTC
Atmosphere Model Location (lat, lon)	(65.0°, -148.0°)	(65.0°, -148.0°)

Table 1. Description of the parameters used in our Monte Carlo simulation, along with the parameters from Berland et al. (2023) upon which our simulation is based.

5 Precipitation Model: Geant4

With backscatter rates constrained by ELFIN data, we now have the ability to directly evaluate the performance of precipitation models. Our approach to precipitation modelling is based on the work of Berland et al. (2023); our model began as a fork from their simulation code. The precipitation model used in this work utilizes Geant4, a kinetic particle simulation code developed by CERN (Agostinelli et al., 2003). Geant4 simulates the interactions of particles with any user-specified material. Here, we utilize Geant4's built-in QBBC physics list, which is the recommended physics list for space radiation applications (Ivantchenko et al., 2012). QBBC includes the effects of bremsstrahlung photon production, an important process at radiation belt energies. For a description of the exact processes and cross sections included in the Geant4 QBBC list, see Section 3 of Berland et al. (2023). No biasing methods such as bremsstrahlung splitting are used in our simulation in order to conserve energy. The parameters used in our model are compared with those used in Berland et al. (2023) in Table 1.

Following the procedure of Berland et al. (2023), we use this model to inject a series of mono-energetic, mono-pitch angle beams consisting of 100,000 electrons each into the atmosphere from above. These beams were simulated every 5 degrees in pitch angle from 0° to 90°, with the exception of the range from 60° to 70°, where beams were

simulated every 1° . This higher resolution accounts for the high sensitivity of backscatter in the pitch angle range surrounding the 100 km loss cone angle ($\approx 67^\circ$ at our injection altitude). The beams were simulated at the center of each of ELFIN's energy channels, from 63 keV to 6500 keV, spaced nearly uniformly in logarithmic space. For each beam, the atmospheric energy deposition and backscattered electron distribution was recorded. A particle was defined as backscattered when it reached the collection altitude with a vertical component of velocity pointed away from the Earth's surface. All backscattered particles were terminated after being recorded. This procedure resulted in a series of tables tabulating the backscatter profiles for a variety of input conditions, forming a set of response functions in energy-pitch angle space that can be combined in a weighted sum scheme to approximate the backscatter of arbitrary input distributions.

6 Model Validation

In order to compare ELFIN data to our Geant4 modelling, we require a procedure to fit the fluxes recorded by ELFIN to the set of lookup tables generated with our Geant4 model. We first integrated each data segment described in Section 3.1 over time to produce an electron distribution in energy-pitch angle space with units of electrons-cm $^{-2}$ -MeV $^{-1}$ -str $^{-1}$. For distributions measured in the Southern hemisphere, the distribution was reversed along the pitch angle axis to match the Geant4 lookup tables, which were simulated in the Northern hemisphere. The fluence measured in each bin was then multiplied by the energy width of the bin and the instrument's geometric factor to retrieve the absolute counts measured by ELFIN at that location. Then, we perform an azimuth correction procedure. This is because our simulation recorded backscatter for all azimuthal angles, while ELFIN was only able to see part of an azimuthal distribution at any given pitch angle. Thus, before we input the data-derived electron counts to the simulation, we multiply the measured counts at each pitch angle by a scaling factor C defined in Equation 3, where Ω is solid angle coverage in steradians, θ_{EPD} is the field of view of the ELFIN detector (22.5°) and α_{bore} is the boresight pitch angle of the ELFIN energetic particle detector. This assumes a uniform azimuthal distribution at a given pitch angle. Figure 7 shows a visual representation of the difference in azimuthal coverage between ELFIN and our simulation.

$$C(\alpha_{\text{bore}}) \equiv \frac{\Omega_{\text{ELFIN}}}{\Omega_{\text{sim}}} = \frac{2\pi(1 - \cos(\frac{\theta_{\text{EPD}}}{2}))}{2\pi(\cos(\alpha_{\text{bore}} - \frac{\theta_{\text{EPD}}}{2}) - \cos(\alpha_{\text{bore}} + \frac{\theta_{\text{EPD}}}{2}))} \quad (3)$$

After scaling the measured fluxes by azimuthal coverage, we find the nearest pitch angle and energy for which a simulation-derived backscatter lookup table exists for each data bin. Each data bin then adds its azimuth-scaled electron count to that lookup table as a weighting factor. If a data-derived bin had pitch angle coverage that brought it within 5° of the 100 km loss cone edge or beyond, it was discarded. This was to avoid the undue influence of trapped particles appearing as if they are in the loss cone and skewing backscatter results, as ELFIN's field of view is not sufficiently small to distinguish trapped particles from precipitating particles near the loss cone edge.

After each eligible data bin assigned its weight to a simulation-derived lookup table, the backscatter from each table was summed by their weight to retrieve a composite backscatter distribution. This composite backscatter was then de-scaled in azimuth by dividing the backscatter at each pitch angle bin by C (Equation 3). Then, similar to our process when cleaning the ELFIN data, any bins with a predicted backscatter with relative error greater than 50% as defined in Equation 1 were set to zero for parity with the calculation of backscatter on ELFIN. After this process, the total electron count in the anti-loss cone for both the predicted backscatter distribution and the ELFIN-measured distribution were summed and recorded. The full process of simulating ELFIN backscatter is illustrated in Figure 8.

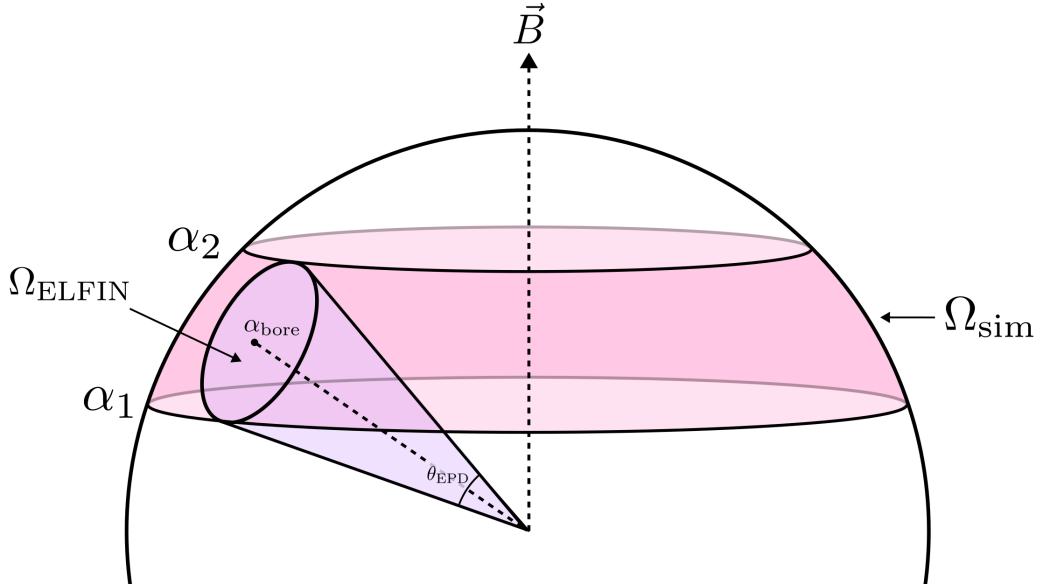


Figure 7. Illustration of the difference in solid angle observed by the satellite (Ω_{ELFIN}) and our simulation (Ω_{sim}) between two pitch angles α_1 and α_2 . The simulation observes all backscatter in a ring between these two pitch angles, while ELFIN can only observe a proportional fraction of this ring. Under the assumption that fluxes are uniform at a given pitch angle across all azimuthal angles, we can utilize a scaling factor (Equation 3) to convert the counts measured by the satellite to the counts present in the full ring and vice versa. Diagram is not to scale.

The process of simulating the backscatter of ELFIN-measured particle distributions was repeated for all data segments that were analyzed in Section 4. For each event, the total anti-loss cone electron counts predicted by our simulation scheme was divided by the measured anti-loss cone electron count, providing a statistic by which we may evaluate the performance of our simulation. These ratios are shown in Figure 9.

From Figure 9, we can see that on average, our simulation is a good estimator of backscatter with the data-model residual distribution centered just above 1. This indicates that there are no systemic biases in our simulation. The order-of-magnitude spread in the distribution can be attributed in part to the resolution of ELFIN's data limiting the accuracy of our modelled inputs to the atmosphere. When modelling backscatter in the very sensitive region within $\sim 10^\circ$ of the loss cone edge, backscatter ratios predicted by our simulation can change by tens of percent over a single degree (see Section 7). With ELFIN's 22.5° field of view, particles from within this sensitive range are assumed to be at the detector's boresight pitch angle. This process of "moving" particles from their unknown true pitch angle to the detector's boresight pitch angle can thus cause a large discrepancy between the particle's true backscatter rate and our estimated backscatter rate. Underestimations of backscatter are caused when a particle that was close to the trapped region is moved to a pitch angle deeper into the loss cone, and overestimations are caused when particles deeper into the loss cone are moved closer to trapped. This issue cannot be avoided without the use of a fitting scheme allowing for interpolation between ELFIN pitch angle bins, which requires assumptions about the pitch angle distribution shape and is out of the scope of this work. We thus believe that this distribution being centered at 1 represents a good first-order validation of our model demonstrating a lack of systemic bias in our model and thus reasonable simulation of the physics of EPP, despite its wide spread.

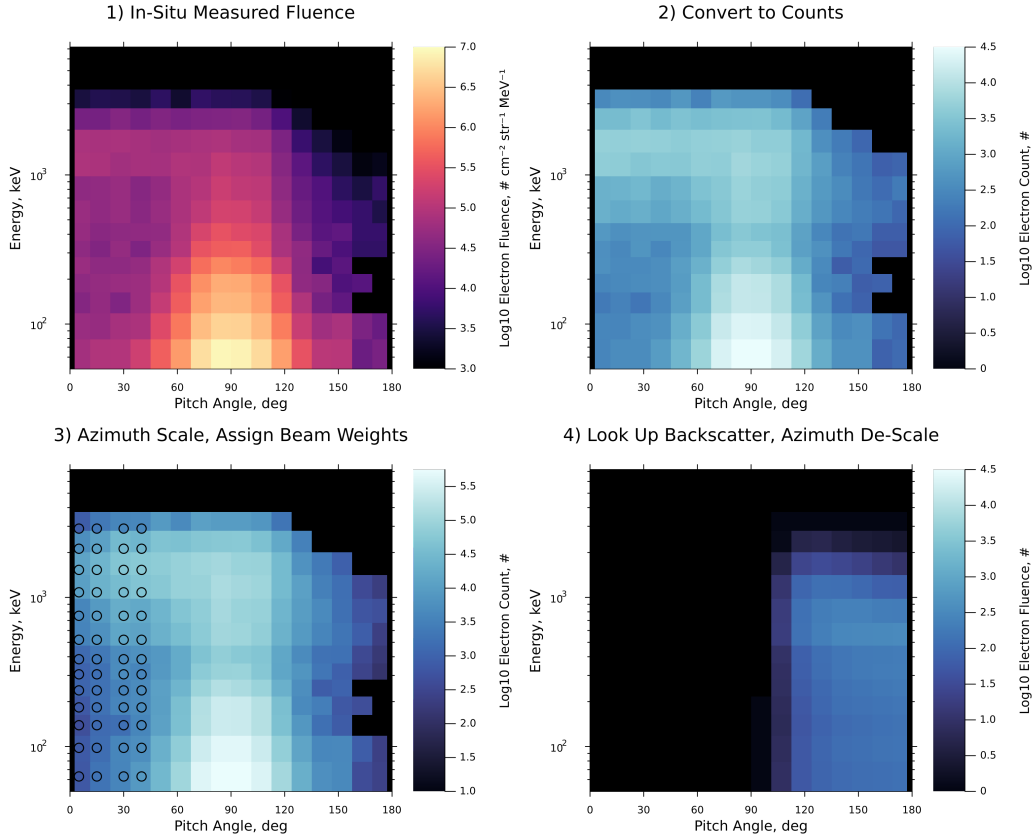


Figure 8. Illustration of the procedure used to fit Geant4 lookup tables to ELFIN data. 1) ELFIN-recorded fluxes are integrated over time for a given data segment to produce differential directional fluence. 2) Each recording bin is multiplied by its energy span and instrument geometric factor to produce measured electron counts. 3) Each data bin in the loss cone is scaled by azimuthal field of view (see text) and assigns its number of counts as a weight to the nearest energy and pitch angle for which a backscatter lookup table exists. Circular markers indicate the location of these lookup tables, and their color indicates their weight in electron counts. Lookup tables with zero weight are not shown for clarity. 4) Backscatter lookup tables are summed by their total weights, de-scaled in azimuthal field of view (see text), and returned.

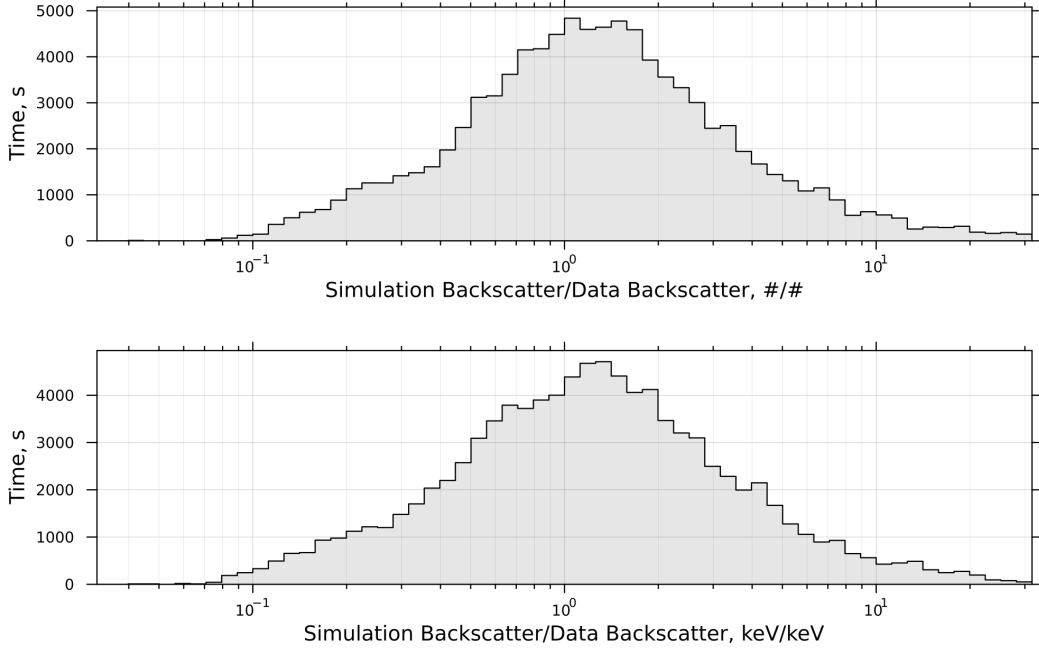


Figure 9. Anti-loss cone electron count predicted by lookup tables derived from our Monte Carlo simulation divided by ELFIN-measured anti-loss cone electron counts for all ELFIN data segments that were analyzed in Section 4. This is based on 26 hours (33,366 spacecraft spins) of data.

7 Simulated Backscatter Characteristics

Using the backscatter lookup tables derived from our Monte Carlo simulation, we can analyze the characteristics of backscatter. In this study, following on the work of (Marshall & Bortnik, 2018), we investigate the pitch angle and energy dependence of backscatter along with the pitch angle distribution of backscattered electrons. Figure 10 illustrates our predicted backscatter ratios as a function of energy and pitch angle. First, we note the extremely sharp increase in backscatter ratio near the 100 km loss cone angle of 67°. When magnetic mirroring was removed from the simulation, this steep gradient disappeared entirely, confirming that the loss cone boundary observed in this simulation is primarily due to the effects of magnetic mirroring. Secondly, we note that the number backscatter is strictly greater than the energy backscatter. This is due to the fact that for a monoenergetic electron beam, electrons can lose energy to the atmosphere but still be backscattered, causing a reduction in energy backscattered without impacting the total number backscattered. On the other hand, it is not possible for an electron to gain energy in the atmosphere in this simulation, meaning that it is not possible for the energy backscatter ratio to exceed the number backscatter ratio for a monoenergetic input beam. The rates and sensitivity of backscatter presented in Figure 10 agree with previous work simulating backscatter (Marshall & Bortnik, 2018; Cotts et al., 2011).

The next parameter of interest is the pitch angle distribution (PAD) of backscattered electron populations. To visualize the dependence of backscattered PADs on pitch angle at a given energy, we calculate the backscattered PAD for each input pitch angle for which we have lookup tables available in units of electrons per steradian. This backscattered PAD is then normalized to integrate to unity over pitch angle for clarity of visualization, putting the PAD in units of electrons per steradian (PAD units) times degrees

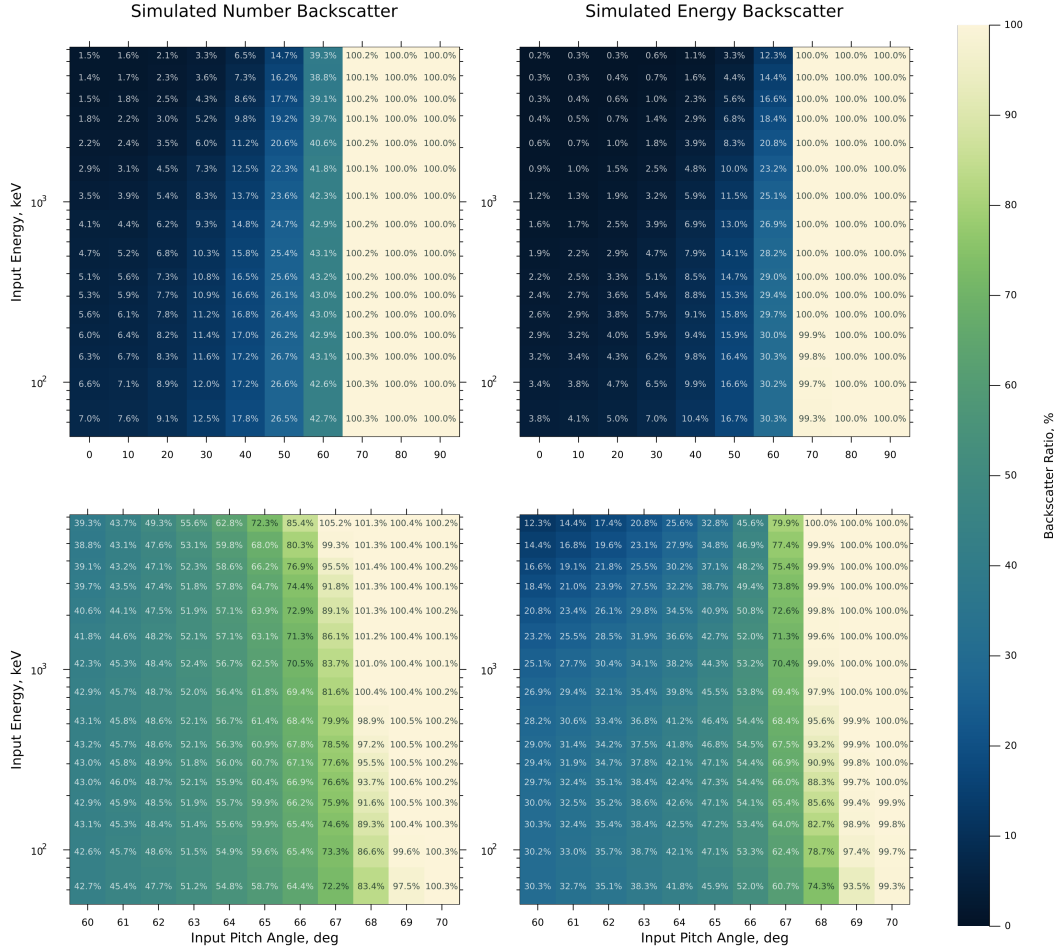


Figure 10. Backscatter ratios for various simulated beams consisting of 100,000 monoenergetic, mono-pitch angle electrons injected into our Geant4 simulation as a function of energy and pitch angle. Electrons were injected into the simulation at 449.5 km and recorded at 450.5 km, where the 100 km loss cone angle is approximately 67° . Left-side panels show number backscatter, and right-side panels show energy backscatter. Top panels show the pitch angle range of 0° to 90° , and bottom panels show a zoomed-in view on the pitch angle range from 60° to 70° .

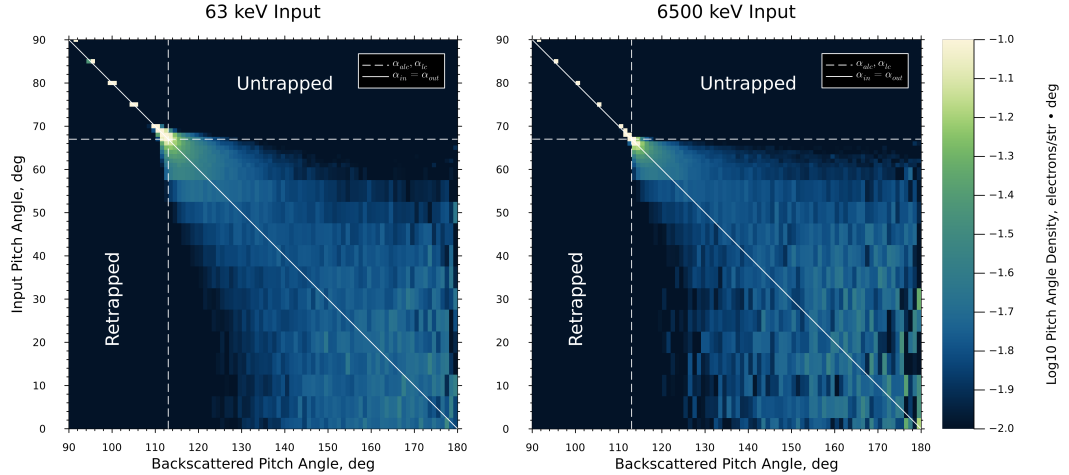


Figure 11. Input pitch angle vs. backscattered pitch angle derived from simulation at a variety of discrete input pitch angles. Each row represents the backscattered pitch angle distribution of a mono-pitch angle, monoenergetic input beam, normalized to solid angle coverage and to integrate to unity. Particles that started in the trapped region and were backscattered in the anti-loss cone are referred to as “untrapped”, and particles that started in the loss cone and were backscattered in the trapped region are referred to as “retrapped”. The 100 km loss cone angle in this simulation is approximately 67° .

(unit from the normalization). This 1D distribution is then plotted horizontally on a heatmap with color representing the density of the distribution. This process was repeated for each input pitch angle at a given energy. The result of this procedure for two input energies is shown in Figure 11.

Figure 11 shows that for input pitch angles deep in the loss cone between approximately 0° and 50° , there is very little sensitivity or correlation between the backscattered PAD and the input pitch angle, with backscattered pitch angle distributions being roughly isotropic between 125° and 180° , and roughly symmetric around the input pitch angle (solid white line). In this range of input pitch angles the nominal magnetic mirror point is far below the surface of the Earth, and thus nearly all backscatter is produced via collisions with atmospheric neutrals altering an electron’s pitch angle sufficiently to escape the atmosphere, accounting for the isotropization of the backscattered distribution. For input angles between approximately 50° and 70° , we begin to see more sensitivity to input pitch angle with the backscattered PAD starting to skew toward the conjugate of the input pitch angle. This represents the regime where magnetic mirroring is beginning to influence the backscatter ratio and there are fewer atmospheric collisions occurring. Since the magnetic mirror point is increasing in altitude with increased input pitch angles (the mirror altitude goes above ground level at inputs around 60°), the pitch angle at any point in the atmosphere is closer to 90° for these inputs than they were for the more field aligned inputs. Thus, it takes fewer collisions to adjust their trajectory to an upgoing direction, resulting in less pitch angle diffusion. This also correlates with the region of input pitch angles where backscattered energy begins to dramatically increase (see Figure 10), further implying a reduction in atmospheric collisions in this region. Within a few degrees of the 100 km mirror point at 67° , magnetic mirroring takes over completely, and these particles never encounter appreciable atmospheric density; thus, the backscattered pitch angle distribution is a nearly-perfect delta function about the magnetic conjugate of the input angle, lying directly on the $\alpha_{in} = \alpha_{out}$ line. We also note that the backscattered PAD does not depend much on energy, except in the

424 approximately 60° to 65° region, where there is slightly more atmospheric scattering for
 425 the high energy beam than the low energy beam, potentially due to the deeper atmo-
 426 spheric penetration of high energy particles owing to their smaller angular deflections
 427 during collisions with neutrals.

428 Next, we observe the pattern of particle movement between regions. A particle that
 429 starts in the trapped region and is backscattered into the anti-loss cone is called “un-
 430 trapped”, and a particle starting in the loss cone and backscattering into the trapped
 431 region is called “retrapped”. Figure 11 shows that there is negligible retrapping and un-
 432 trapping in our simulation, with the vast majority of particles remaining in the region
 433 they started in (either the trapped region or the loss/anti-loss cone). There is a minor
 434 energy dependence to this observation, with the cutoff point varying by about 5° between
 435 the 63 keV input and the 6.5 MeV input. This energy dependence is consistent with pre-
 436 vious work (Marshall & Bortnik, 2018). Moreover, we conclude that this predicts that
 437 using in-situ measurements of loss cone and anti-loss cone fluxes as a proxy measurement
 438 for precipitating and backscattered fluxes respectively is highly accurate.

439 The pitch angle distributions of backscattered electron beams has also been reported
 440 in Cotts et al. (2011); Marshall and Bortnik (2018), and Berland et al. (2023). The pitch
 441 angle distributions reported in Cotts et al. (2011) and Marshall and Bortnik (2018) (Fig-
 442 ure 3 in both papers) show a very similar trend to our results, with field-aligned inputs
 443 having isotropized backscatter with a rapid transition to a delta function near the 100 km
 444 loss cone edge, with a slight energy dependence. Berland et al. (2023) predicts different
 445 pitch angle distributions (Figure 7 in their paper) that do not approach delta functions
 446 near the loss cone edge. This likely indicates a magnetic field configuration in their sim-
 447 ulation that does not include magnetic mirroring.

448 Overall, we find that our simulation work agrees with previous modelling efforts
 449 and has been validated with in-situ data from the ELFIN mission.

450 8 Conclusions

451 Backscatter is an important part of the interconnected atmosphere-ionosphere-magnetosphere
 452 system. In this paper, we have used in-situ data from the ELFIN satellites to constrain
 453 EPP backscatter rates and have found that the backscatter ratio of precipitating elec-
 454 trons is primarily a function of the strength of loss cone filling. Backscatter rates were
 455 at or below 10% for the strongest filling of the loss cone ($J_{\text{prec}}/J_{\text{trap}} > 1$), increasing
 456 up to approximately 60% during periods with little to no loss cone filling. This varia-
 457 tion is attributed to the pitch angle dependence of backscatter rates, with strong loss
 458 cone filling representing the backscatter rates deep in the loss cone and weak loss cone
 459 filling representing the backscatter rates near the edge of the loss cone.

460 We then introduced an updated EPP backscatter model which was used to sim-
 461 ulate all ELFIN data that was used in the backscatter analysis. This model showed no
 462 systemic biases. There is noticeable spread in its predictions of backscatter compared
 463 to ELFIN that we attribute to the highly-sensitive nature of backscatter dynamics near
 464 the loss cone edge in combination with limitations of the ELFIN field of view, as it is
 465 unable to resolve the loss cone edge at the characteristic pitch angle scale over which backscat-
 466 ter rates change, typically a few degrees or less at LEO.

467 Finally, we used our precipitation model to characterize the sensitivities and pitch
 468 angle distributions of backscatter. We found that backscatter is generally much more sen-
 469 sitive to input pitch angle than input energy, as previous work has shown. We found that
 470 backscatter is dominated by atmospheric interactions at more field aligned pitch angles,
 471 which isotropizes the backscattered pitch angle distribution in the anti-loss cone. In the
 472 region near the loss cone angle, magnetic mirroring begins to dominate over atmospheric
 473 interactions, leading to a backscattered pitch angle distribution that trends towards a

474 delta function as the input pitch angle approaches the trapped region. We also found
 475 that particles that start in the trapped region are almost exclusively backscattered in
 476 the trapped region, and particles that start in the loss cone are almost exclusively backscat-
 477 tered in the anti-loss cone. These results suggest that very few interactions occur above
 478 100 km for these particle energies. From these results, we conclude that measured fluxes
 479 in the loss cone and anti-loss cone are good proxies for precipitating and backscattered
 480 populations respectively when measuring in-situ particle distributions.

481 8.1 Caveats and Future Work

482 The primary limitation of our model-data comparison is a lack of high-resolution
 483 data in sensitive regions of the pitch angle distribution, i.e. very near the loss cone, where
 484 resolution on the order of one degree is necessary to accurately characterize the precip-
 485 itating and trapped populations. This limitation could possibly be avoided through the
 486 use of a fitting scheme. Such a scheme would utilize the recorded pitch angle and energy
 487 distribution and make an assumption for the driver of the precipitation. This driver could
 488 then be fed to a set of lookup tables containing archetypal pitch angle distributions for
 489 that driver. For example, Figure 3 in Capannolo et al. (2023) shows physics-based pitch
 490 angle distributions for EMIC-driven precipitation measured on ELFIN. These pitch an-
 491 gle curves could then be fitted to ELFIN’s recorded flux and sampled at an arbitrarily
 492 high resolution. By predicting the shape of the pitch angle distribution in the sensitive
 493 region near the loss cone edge rather than assuming a stepped distribution based on the
 494 measured flux, we may recover a more accurate prediction of backscatter. This, however,
 495 introduces other uncertainties through the incorporation of other models to assume an
 496 underlying pitch angle distribution.

497 It is also possible to interpolate our backscatter lookup tables between nearby sim-
 498 ulation runs to obtain backscattered particle distributions on a higher-resolution grid than
 499 the beams we calculated, as done in Cotts et al. (2011). Given the smooth variance of
 500 the backscatter parameters presented in this paper, interpolation would be a reasonable
 501 approach to produce a higher-fidelity backscatter model without excessive computational
 502 effort. In the trapped region, this interpolation would likely be as simple as assuming
 503 pure adiabatic mirroring at the conjugate pitch angle to the input angle, while a more
 504 complicated scheme would be required for the loss and anti-loss cones.

505 Open Research Section

506 ELFIN data is available for free at <https://data.elfin.ucla.edu/ela/>. Geant4
 507 is available for free from <https://geant4.web.cern.ch/download/11.3.2.html>. The
 508 Geant4 code used to generate lookup tables is available for free at <https://github.com/julia-claxton/g4epp-source/tree/main>. The backscatter lookup tables generated
 509 by the Geant4 simulation are available for free at [TODO: lookup tables zenodo].
 510 All code used to perform the analysis and generate figures, as well as the list of ELFIN
 511 events used in the analysis, is available for free at [TODO: project repo].

513 Acknowledgments

514 The authors acknowledge the Ethan Tsai and the ELFIN team for providing data and
 515 technical support, the Julia programming language team (Bezanson et al., 2017) for the
 516 use of the Julia language, the SpacePy Python package (Niekof et al., 2022; Steven K. Mor-
 517 ley et al., 2010) for the use of their tools, and University of Colorado Research Comput-
 518 ing for the use of their high-performance computing resources and assistance in troubleshoot-
 519 ing.

520 **References**

- 521 Agostinelli, S., Allison, J., Amako, K. a., Apostolakis, J., Araujo, H., Arce, P., ...
 522 others (2003). Geant4—a simulation toolkit. *Nuclear instruments and meth-*
 523 *ods in physics research section A: Accelerators, Spectrometers, Detectors and*
 524 *Associated Equipment*, 506(3), 250–303.
- 525 Angelopoulos, V., Tsai, E., Bingley, L., Shaffer, C., Turner, D. L., Runov, A., ...
 526 Zhang, G. Y. (2020, 7 30). The ELFIN Mission. *Space Science Reviews*,
 527 216(5), 103. Retrieved from <https://doi.org/10.1007/s11214-020-00721-7>
 528 doi: 10.1007/s11214-020-00721-7
- 529 Banks, P., & Nagy, A. (1970). Concerning the influence of elastic scattering upon
 530 photoelectron transport and escape. *Journal of Geophysical Research*, 75(10),
 531 1902–1910.
- 532 Banks, P. M., Chappell, C. R., & Nagy, A. F. (1974). A new model for the
 533 interaction of auroral electrons with the atmosphere: Spectral degra-
 534 dation, backscatter, optical emission, and ionization. *Journal of Geophysi-*
 535 *cal Research (1896-1977)*, 79(10), 1459–1470. Retrieved from <https://agupubs.onlinelibrary.wiley.com/doi/abs/10.1029/JA079i010p01459>
 536 doi: <https://doi.org/10.1029/JA079i010p01459>
- 537 Berger, M. J., Seltzer, S. M., & Maeda, K. (1974). Some new results on electron
 538 transport in the atmosphere. *Journal of Atmospheric and Terrestrial Physics*,
 539 36(4), 591–617.
- 540 Berland, G. D., Marshall, R. A., Capannolo, L., McCarthy, M. P., & Zheng,
 541 L. (2023). Kinetic modeling of radiation belt electrons with geant4
 542 to study energetic particle precipitation in earth's atmosphere. *Earth*
 543 *and Space Science*, 10(11), e2023EA002987. Retrieved from <https://agupubs.onlinelibrary.wiley.com/doi/abs/10.1029/2023EA002987>
 544 (e2023EA002987 2023EA002987) doi: <https://doi.org/10.1029/2023EA002987>
- 545 Bezanson, J., Edelman, A., Karpinski, S., & Shah, V. B. (2017). Julia: A fresh ap-
 546 proach to numerical computing. *SIAM Review*, 59(1), 65–98. Retrieved from
 547 <https://epubs.siam.org/doi/10.1137/141000671> doi: 10.1137/141000671
- 548 Capannolo, L., Li, W., Ma, Q., Qin, M., Shen, X.-C., Angelopoulos, V., ...
 549 Hanzelka, M. (2023). Electron precipitation observed by elfin using proton
 550 precipitation as a proxy for electromagnetic ion cyclotron (emic) waves. *Geo-*
 551 *physical Research Letters*, 50(21), e2023GL103519. Retrieved from <https://agupubs.onlinelibrary.wiley.com/doi/abs/10.1029/2023GL103519>
 552 (e2023GL103519 2023GL103519) doi: <https://doi.org/10.1029/2023GL103519>
- 553 Cotts, B. R., Inan, U. S., & Lehtinen, N. G. (2011). Longitudinal dependence of
 554 lightning-induced electron precipitation. *Journal of Geophysical Research:*
 555 *Space Physics*, 116(A10).
- 556 Cummings, W., LaQuey, R., O'Brien, B. J., & Walt, M. (1966). Rocket-borne mea-
 557 surements of particle fluxes and auroral light. *Journal of Geophysical Research*,
 558 71(5), 1399–1407.
- 559 Davidson, G., & Walt, M. (1977). Loss cone distributions of radiation belt electrons.
 560 *Journal of Geophysical Research*, 82(1), 48–54.
- 561 Feinland, M., Blum, L. W., Marshall, R. A., Gan, L., Shumko, M., & Looper, M.
 562 (2024). Lightning-induced relativistic electron precipitation from the inner
 563 radiation belt. *Nature Communications*, 15(1), 8721.
- 564 Funke, B., López-Puertas, M., Stiller, G. P., & von Clarmann, T. (2014). Mesos-
 565 pheric and stratospheric no produced by energetic particle precipitation dur-
 566 ing 2002–2012. *Journal of Geophysical Research: Atmospheres*, 119(7), 4429–
 567 4446. Retrieved from <https://agupubs.onlinelibrary.wiley.com/doi/abs/10.1002/2013JD021404>
 568 doi: <https://doi.org/10.1002/2013JD021404>
- 569 Ivantchenko, A. V., Ivanchenko, V. N., Molina, J.-M. Q., & Incerti, S. L. (2012).
 570 Geant4 hadronic physics for space radiation environment. *Inter-
 571 International Journal of Radiation Biology*, 88(1-2), 171–175. Retrieved from
 572 <https://doi.org/10.1080/09553002.2012.670300>

- 575 <https://doi.org/10.3109/09553002.2011.610865> (PMID: 21830895)
576 doi: 10.3109/09553002.2011.610865

577 Juarez Madera, D., Marshall, R. A., Elschot, S., Kaepller, S., Reyes, P., Var-
578 ney, R. H., & Crew, A. B. (2023). Time-dependent inversion of energetic
579 electron precipitation spectra from ground-based incoherent scatter radar
580 measurements. *Journal of Geophysical Research: Space Physics*, 128(5),
581 e2022JA031000.

582 Khazanov, G. V., & Chen, M. W. (2021). Why atmospheric backscatter is important
583 in the formation of electron precipitation in the diffuse aurora. *Journal of Geo-
584 physical Research: Space Physics*, 126(5), e2021JA029211.

585 Koskinen, H. E. J., & Kilpua, E. K. J. (2022). Dynamics of the electron belts.
586 In *Physics of earth's radiation belts: Theory and observations* (pp. 213–240).
587 Cham: Springer International Publishing. Retrieved from https://doi.org/10.1007/978-3-030-82167-8_7 doi: 10.1007/978-3-030-82167-8_7

588 Lejeune, G. (1979). “two-stream” photoelectron distributions with interhemispheric
589 coupling: A mixing of analytical and numerical methods. *Planetary and Space
590 Science*, 27(5), 561–576.

591 Maeda, K. (1965). *Diffusion of auroral electrons in the atmosphere* (Vol. 2612). National
592 Aeronautics and Space Administration.

593 Mantas, G. P., & Walker, J. C. (1976). The penetration of soft electrons into the
594 ionosphere. *Planetary and Space Science*, 24(5), 409–423.

595 Marshall, R. A., & Bortnik, J. (2018). Pitch angle dependence of energetic electron
596 precipitation: Energy deposition, backscatter, and the bounce loss cone. *Journal
597 of Geophysical Research: Space Physics*, 123(3), 2412–2423. Retrieved
598 from <https://agupubs.onlinelibrary.wiley.com/doi/abs/10.1002/2017JA024873>
599 doi: <https://doi.org/10.1002/2017JA024873>

600 McDiarmid, I. B., Rose, D. C., & Budzinski, E. (1961). Direct measurement of
601 charged particles associated with auroral zone radio absorption. *Canadian
602 Journal of Physics*, 39(12), 1888–1900. Retrieved from <https://doi.org/10.1139/p61-210>
603 doi: 10.1139/p61-210

604 Millan, R., & Thorne, R. (2007). Review of radiation belt relativistic electron
605 losses. *Journal of Atmospheric and Solar-Terrestrial Physics*, 69(3), 362–377.
606 Retrieved from <https://www.sciencedirect.com/science/article/pii/S1364682606002768> (Global Aspects of Magnetosphere-Ionosphere Coupling)
607 doi: <https://doi.org/10.1016/j.jastp.2006.06.019>

608 Miyoshi, Y., Oyama, S., Saito, S., Kurita, S., Fujiwara, H., Kataoka, R., ... others
609 (2015). Energetic electron precipitation associated with pulsating aurora: Eis-
610 cat and van allen probe observations. *Journal of Geophysical Research: Space
611 Physics*, 120(4), 2754–2766.

612 Niehof, J. T., Morley, S. K., Welling, D. T., & Larsen, B. A. (2022). The spacepy
613 space science package at 12 years. *Frontiers in Astronomy and Space Sciences*,
614 Volume 9 - 2022. Retrieved from <https://www.frontiersin.org/journals/astronomy-and-space-sciences/articles/10.3389/fspas.2022.1023612>
615 doi: 10.3389/fspas.2022.1023612

616 O’Brien, B. J. (1962). Lifetimes of outer-zone electrons and their precipitation into
617 the atmosphere. *Journal of Geophysical Research (1896-1977)*, 67(10), 3687–
618 3706. Retrieved from <https://agupubs.onlinelibrary.wiley.com/doi/abs/10.1029/JZ067i010p03687>
619 doi: <https://doi.org/10.1029/JZ067i010p03687>

620 O’Brien, B. J. (1964). High-latitude geophysical studies with satellite in-
621 jun 3: 3. precipitation of electrons into the atmosphere. *Journal of Geo-
622 physical Research (1896-1977)*, 69(1), 13–43. Retrieved from <https://agupubs.onlinelibrary.wiley.com/doi/abs/10.1029/JZ069i001p00013>
623 doi: <https://doi.org/10.1029/JZ069i001p00013>

624 Randall, C. E., Harvey, V. L., Manney, G. L., Orsolini, Y., Codrescu, M., Sioris,
625 C., ... Russell III, J. M. (2005). Stratospheric effects of energetic particle

- 630 precipitation in 2003–2004. *Geophysical Research Letters*, 32(5). Retrieved
 631 from <https://agupubs.onlinelibrary.wiley.com/doi/abs/10.1029/2004GL022003>
 632 doi: <https://doi.org/10.1029/2004GL022003>
- 633 Richards, P. G., & Peterson, W. (2008). Measured and modeled backscatter of iono-
 634 spheric photoelectron fluxes. *Journal of Geophysical Research: Space Physics*,
 635 113(A8).
- 636 Ripoll, J.-F., Claudepierre, S., Ukhorskiy, A., Colpitts, C., Li, X., Fennell, J., &
 637 Crabtree, C. (2020). Particle dynamics in the earth's radiation belts: Review
 638 of current research and open questions. *Journal of Geophysical Research: Space
 639 Physics*, 125(5), e2019JA026735.
- 640 Sanchez, E. R., Ma, Q., Xu, W., Marshall, R. A., Bortnik, J., Reyes, P., ... Kaep-
 641 pler, S. (2022). A test of energetic particle precipitation models using simul-
 642 taneous incoherent scatter radar and van allen probes observations. *Journal of
 643 Geophysical Research: Space Physics*, 127(8), e2021JA030179.
- 644 Seppälä, A., Verronen, P. T., Clilverd, M. A., Randall, C. E., Tamminen, J., Sofieva,
 645 V., ... Kyrölä, E. (2007). Arctic and antarctic polar winter no and energetic
 646 particle precipitation in 2002–2006. *Geophysical Research Letters*, 34(12).
 647 Retrieved from <https://agupubs.onlinelibrary.wiley.com/doi/abs/10.1029/2007GL029733>
 648 doi: <https://doi.org/10.1029/2007GL029733>
- 649 Sinnhuber, M., Nieder, H., & Wieters, N. (2012, 11 01). Energetic particle precipita-
 650 tion and the chemistry of the mesosphere/lower thermosphere. *Surveys in Geo-
 651 physics*, 33(6), 1281–1334. Retrieved from <https://doi.org/10.1007/s10712-012-9201-3>
 652 doi: 10.1007/s10712-012-9201-3
- 653 Solomon, S. C. (2001). Auroral particle transport using monte carlo and hybrid
 654 methods. *Journal of Geophysical Research: Space Physics*, 106(A1), 107–116.
- 655 Steven K. Morley, Daniel T. Welling, Josef Koller, Brian A. Larsen, Michael G. Hen-
 656 derson, & Jonathan Niehof. (2010). SpacePy - A Python-based Library
 657 of Tools for the Space Sciences. In Stéfan van der Walt & Jarrod Millman
 658 (Eds.), *Proceedings of the 9th Python in Science Conference* (p. 67 - 72). doi:
 659 10.25080/Majora-92bf1922-00c
- 660 Tsai, E. (2025, 5 8). Personal Communication.
- 661 Tsyganenko, N. (1987). Global quantitative models of the geomagnetic field
 662 in the cislunar magnetosphere for different disturbance levels. *Plane-
 663 tary and Space Science*, 35(11), 1347–1358. Retrieved from <https://www.sciencedirect.com/science/article/pii/0032063387900468>
 664 doi: [https://doi.org/10.1016/0032-0633\(87\)90046-8](https://doi.org/10.1016/0032-0633(87)90046-8)
- 665 Turunen, E., Kero, A., Verronen, P. T., Miyoshi, Y., Oyama, S.-I., & Saito, S.
 666 (2016). Mesospheric ozone destruction by high-energy electron precipitation as-
 667 sociated with pulsating aurora. *Journal of Geophysical Research: Atmospheres*,
 668 121(19), 11–852.
- 669 Walt, M., MacDonald, W. M., & Francis, W. E. (1968). Penetration of auroral
 670 electrons into the atmosphere. In *Physics of the magnetosphere: Based upon
 671 the proceedings of the conference held at boston college june 19–28, 1967* (pp.
 672 534–555).
- 673 Wetzel, W., Sample, J., Engel, E., & Shumko, M. (2024). Properties of
 674 relativistic bouncing microbursts. *Journal of Geophysical Research: Space
 675 Physics*, 129(6), e2023JA032344. Retrieved from <https://agupubs.onlinelibrary.wiley.com/doi/abs/10.1029/2023JA032344>
 676 (e2023JA032344 2023JA032344) doi: <https://doi.org/10.1029/2023JA032344>